Institute of Physics Publishing
doi:10.1088/1742-6596/7/1/014
Journal of Physics: Conference Series **7** (2005) 163–173
Chaotic Transport and Complexity in Fluids and Plasmas

Derivation of an analytical area-preserving map to describe transport barriers in tokamaks

Marisa Roberto

Instituto Tecnológico de Aeronáutica, Centro Técnico Aeroespacial, Departamento de Física, 12228-900, São José dos Campos, São Paulo, Brazil

Elton César da Silva, Iberê Luiz Caldas

Instituto de Física, Universidade de São Paulo, 05315-970, São Paulo, São Paulo, Brazil

Ricardo Luiz Viana [1]

Departamento de Física, Universidade Federal do Paraná, 81531-990, Curitiba, Paraná, Brazil.

Abstract. Transport barriers have been observed in tokamak experiments involving negative magnetic shear. The use of non-twist maps has been proposed in order to explain the underlying dynamical mechanism of such barriers. In this work we derive an area-preserving analytical map to describe the formation of a transport barrier in a chaotic field line region of a tokamak with an ergodic magnetic limiter. The map so obtained is used to investigate the radial diffusion of field lines in such a configuration.

1. Introduction

The existence of closed magnetic surfaces is a necessary condition for plasma confinement in fusion schemes [1, 2, 3]. Magnetic flux surfaces with the topology of nested tori exist whenever the system possesses a spatial symmetry and, accordingly, such surfaces may be partially or entirely destroyed as this symmetry is broken by some means [4, 5, 6]. Particle confinement in fusion plasma is related in a non-trivial way with the determination of magnetic surfaces. Classical and neoclassical transport in directions perpendicular to these surfaces, for example, is not sufficient to explain the experimental data [7, 8]. The observed anomalous transport is one of the most studied themes in fusion plasma theory [9].

There are two general points of view on anomalous diffusion: (i) the existence of magnetic surfaces is assumed, but the transport properties are due to complex particle motions which are disregarded in traditional theories [2, 3]; (ii) the particle orbits are taken as essentially simple, but the magnetic surfaces themselves may not exist [10, 11]. We shall assume the latter view, and consider that the existence of a layer of chaotic, volume-filling magnetic field lines should be found as a result of the destruction of equilibrium flux surfaces by means of various mechanisms, as error fields, internal instabilities, or externally applied resonant fields [4].

However, it is generally not true that chaotic layers of magnetic field lines lead necessarily to a uniform spread of particle and energy fluxes in radial directions. The underlying structure of chaotic motion, represented by a complex tapestry of homoclinic and heteroclinic intersections of invariant manifolds of

[1] Corresponding author. e-mail: viana@fisica.ufpr.br

unstable periodic orbits, may lead to observable consequences on the transport properties of the magnetic field lines. One of such effects is the creation of transport barriers which reduce radial diffusion in a given chaotic magnetic field region, yielding a diminishing particle and energy escape at the plasma edge.

Transport barriers have been observed in advanced tokamak scenarios characterized by a negative magnetic shear region within the plasma column [12, 13]. Such regions can be created by means of a non-peaked plasma current density, leading to a non-monotonic radial profile for the safety factor [14]. Area-preserving Poincaré maps of magnetic field lines in situations with negative shear configurations are described by non-twist maps, for which the non-degeneracy condition for the Kolmogorov-Arnold-Moser (KAM) theorem to be valid is not generally fulfilled [4, 15]. Non-twist maps present some peculiar features, with respect to traditionally used twist maps [16, 17]. For example, it may happen that two neighbor island chains approach each other without having been destroyed and coalesce through a (non-resistive) reconnection process [18]. The transport barrier arises from a combination of typical features of non-twist maps: reconnection and bifurcation, occurring in the reversed shear region, which have been considered to explain some features of anomalous diffusion observed in tokamak advanced scenarios [19, 20, 21].

In this paper we present a derivation of an analytical non-twist map to describe the formation of a transport barrier in a tokamak. The external field responsible for the required destruction of equilibrium flux surfaces will be generated by an ergodic magnetic limiter [22, 23, 24, 25]. This perturbing field will be superposed to the tokamak equilibrium field with a negative shear region due to a non-peaked plasma current [21]. The map derived in this work can be used to numerically evidence the formation of a transport barrier due to a reconnection-bifurcation mechanism, and its effect on the plasma transport can be inferred from the study of field line diffusion. The paper is organized as follows: in section II we present the equilibrium and perturbing fields. Section III shows the area-preserving non-twist map obtained for two resonant perturbations. Section IV deals with the transport barrier resulting from the magnetic field line structure. Our conclusions are left to the last section.

2. Theoretical model

In the following we choose to work with a polar-toroidal coordinate system in the tokamak: $(r_t, \theta_t, \varphi_t)$, given by [26]

$$r_t = \frac{R_0'}{\cosh\xi - \cos\omega}, \qquad \theta_t = \pi - \omega, \qquad \varphi_t = \Phi, \tag{1}$$

in terms of the more familiar toroidal coordinates (ξ, ω, Φ) which, on their hand, are defined from the circular-cylindrical coordinates (R, φ, Z) by

$$R = \frac{R_0' \sinh\xi}{\cosh\xi - \cos\omega}, \qquad Z = \frac{R_0' \sin\omega}{\cosh\xi - \cos\omega}, \tag{2}$$

where R_0' is the major radius of the circular centre (i.e., the magnetic axis radius). In this coordinate system ω has the meaning of a poloidal angle, and ξ is related to the distance from the circular centre. The polar-toroidal coordinates (1) can also be given by their expression in terms of the local tokamak coordinates (r, θ, φ):

$$r_t = r\left[1 - \frac{r}{R_0'}\cos\theta + \left(\frac{r}{2R_0'}\right)^2\right]^{1/2}, \tag{3}$$

$$\sin\theta_t = \sin\theta\left[1 - \frac{r}{R_0'}\cos\theta + \left(\frac{r}{2R_0'}\right)^2\right]^{-1/2}, \tag{4}$$

such that, in the large aspect ratio limit ($r_t \ll R_0'$), r_t and θ_t become r and θ, respectively.

The model equilibrium field $\mathbf{B}_0$ is calculated from the poloidal flux and current functions, $\Psi_p(r_t, \theta_t)$ and $I(r_t, \theta_t)$ respectively, by

$$B_0{}^1 = -\frac{1}{R'_0 r_t}\frac{\partial \Psi_p}{\partial \theta_t}, \tag{5}$$

$$B_0{}^2 = \frac{1}{R'_0 r_t}\frac{\partial \Psi_p}{\partial r_t}, \tag{6}$$

$$B_0{}^3 = -\frac{\mu_0 I}{R^2}, \tag{7}$$

where

$$R^2 = {R'_0}^2\left[1 - 2\frac{r_t}{R'_0}\cos\theta_t - \left(\frac{r_t}{R'_0}\right)^2 \sin^2\theta_t\right]. \tag{8}$$

and Ψ_p is obtained from an approximated analytical solution of the Grad-Schlüter-Shafranov equation in these coordinates [26]:

$$\frac{1}{r_t}\frac{\partial}{\partial r_t}\left(r_t\frac{\partial \Psi_p}{\partial r_t}\right) + \frac{1}{r_t^2}\frac{\partial^2 \Psi_p}{\partial \theta_t^2} = \mu_0 J_3(\Psi_p) + \mu_0 {R'_0}^2\frac{dp}{d\Psi_p}\left(2\frac{r_t}{R'_0}\cos\theta_t + \frac{r_t^2}{{R'_0}^2}\sin^2\theta_t\right) + \\ + \frac{r_t}{R'_0}\left[\cos\theta_t\left(2\frac{\partial^2 \Psi_p}{\partial r_t^2} + \frac{1}{r_t}\frac{\partial \Psi_p}{\partial r_t}\right) + \sin\theta_t\left(\frac{1}{r_t^2}\frac{\partial \Psi_p}{\partial \theta_t} - \frac{2}{r_t}\frac{\partial^2 \Psi_p}{\partial \theta_t \partial r_t}\right)\right], \tag{9}$$

where J_3 is the toroidal current density, given by

$$J_3(\Psi_p) = -{R'_0}^2\frac{dp}{d\Psi_p} - \frac{d}{d\Psi_p}\left(\frac{1}{2}\mu_0 I^2\right), \tag{10}$$

in terms of the pressure p.

The approximate solution of Eq. (9) is written as

$$\Psi_p(r_t, \theta_t) = \Psi_{p0}(r_t) + \delta\Psi_p(r_t, \theta_t), \tag{11}$$

with $|\delta\Psi_p(r_t, \theta_t)| \ll |\Psi_{p0}(r_t)|$, and where Ψ_{p0} is obtained by considering a reversed shear equilibrium characterized by a toroidal current density profile with a central hole [27], in such a way that

$$\frac{d\Psi_{p0}(r_t)}{dr_t} = \frac{\mu_0 I_p R'_0}{2\pi r_t}\left[1 - \left(1 + \beta'\frac{r_t^2}{a^2}\right)\left(1 - \frac{r_t^2}{a^2}\right)^{\gamma+1}\right], \tag{12}$$

with a as the plasma radius, determined by a material limiter, and $\beta' \equiv \beta(\gamma+1)/(\beta+\gamma+2)$, where β and γ are positive parameters. We normalize the minor tokamak radius b_t, and the plasma radius a to the major (magnetic axis) radius R'_0, such that $a/R'_0 = 0.25$ and $b/R'_0 = 0.33$ [24]. We also choose $q(a) = 4.04$ and $q(0) = 3.50$, corresponding to the safety factors at the plasma edge and magnetic axis, respectively, as observed in typical discharges with negative magnetic shear, for which $\beta = 3.0$ and $\gamma = 1.0$. Some equilibrium flux surfaces are depicted in Figure 1.

An important consequence of adopting such a hollow plasma profile is that the safety factor of the magnetic surfaces [24]

$$q(r_t) = \frac{1}{2\pi}\int_0^{2\pi}\frac{B^0_{\varphi_t}(r_t, \theta_t)}{B^0_{\theta_t}(r_t)}d\theta_t, \tag{13}$$

has a non-monotonic profile. For some values of the safety factor there are two magnetic surfaces with different radii r_1 and r_2. The shearless radius r_s is defined by $(dq/dr)(r_s) = 0$, such that $r_1 < r_s < r_2$.

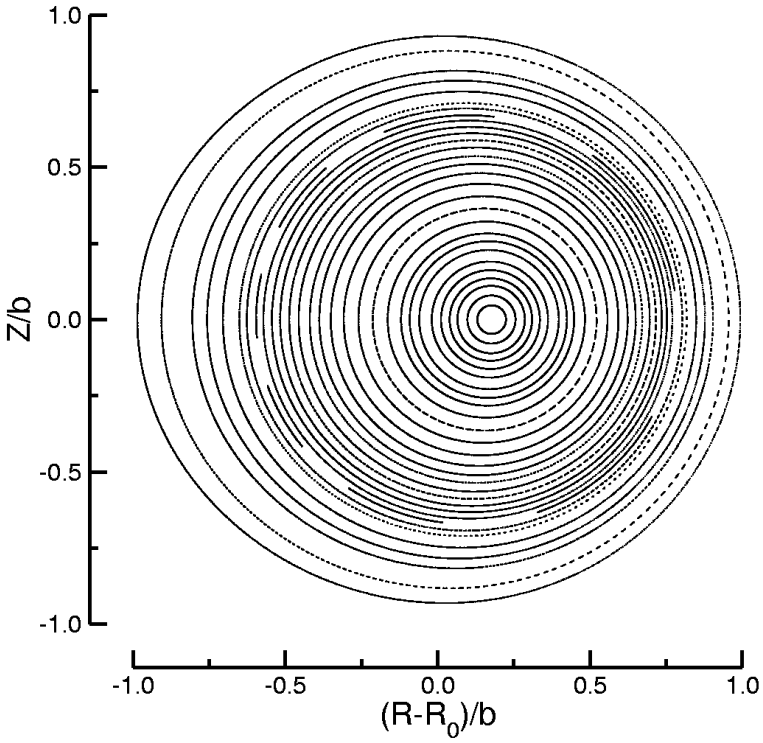

Figure 1. Equilibrium flux surfaces.

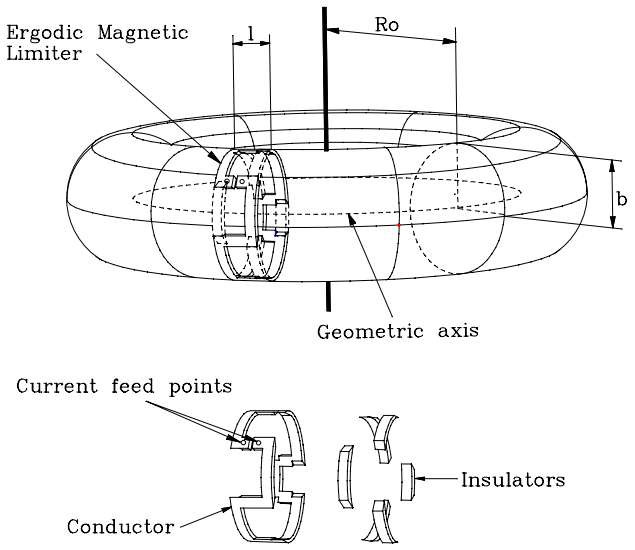

Figure 2. Scheme of an ergodic magnetic limiter.

As is well-known from Hamiltonian dynamics, a general magnetostatic perturbation of the equilibrium will create a multitude of pendular islands of various widths at every rational surface (namely, where the safety factor is the ratio of two coprime integers) [4]. However, if the perturbation is resonant with some rational flux surface, the islands are more pronounced at the position of the resonant surface. Non-monotonic safety profiles are thus likely to present two neighbor island chains near the shearless radius.

An example of magnetostatic perturbation of considerable theoretical and experimental interest is that provided by an ergodic magnetic limiter, which consists of N_r current rings of length ℓ located symmetrically along the toroidal direction of the tokamak [Figure 2]. These current rings may be regarded as slices of a pair of external helical windings located at $r_t = b_t$, conducting a current I_h in opposite senses for adjacent conductors, and satisfying a winding law [24] $u_t = m_0\theta_t - n_0\varphi_t =$ constant. We choose $N_r = 4$ rings with mode numbers $(m_0, n_0) = (3, 1)$.

The perturbing magnetic field $\mathbf{B}^1$ produced by such a configuration has been calculated elsewhere [24], and reads

$$B_L^1 = -\frac{1}{R_0' r_t}\frac{\partial A_{L3}}{\partial \theta_t}, \tag{14}$$

$$B_L^2 = \frac{1}{R_0' r_t}\frac{\partial A_{L3}}{\partial r_t}, \tag{15}$$

where

$$A_{L3}(r_t, \theta_t, \varphi_t) = -\frac{\mu_0 I_h R_0'}{\pi}\left(\frac{r_t}{b_t}\right)^{m_0} \exp\left\{i\left[(m_0)\,\theta_t - n_0\varphi_t\right]\right\}, \tag{16}$$

The magnetic field line equations

$$(\mathbf{B}^0 + \mathbf{B}_1) \times \mathbf{d}\ell = \mathbf{0} \tag{17}$$

can be written in a Hamiltonian form [28]

$$\frac{d\mathcal{I}}{dt} = -\frac{\partial \mathcal{H}}{\partial \vartheta}, \qquad \frac{d\vartheta}{dt} = \frac{\partial \mathcal{H}}{\partial \mathcal{I}}, \tag{18}$$

where $(\mathcal{I}, \vartheta)$ are the action-angle variables of a Hamiltonian $\mathcal{H}$, and the azimuthal angle, $\varphi_t = t$, has been set as a time-like variable. The Hamiltonian for the system can be splited, as usual, as the sum of an integrable and a perturbing term

$$\mathcal{H}(\mathcal{I}, \vartheta, t) = \mathcal{H}_0(\mathcal{I}) + \frac{\ell}{R_0'}\mathcal{H}_1(\mathcal{I}, \vartheta, t)\sum_{k=-\infty}^{+\infty}\delta\left(t - k\frac{2\pi}{N_a}\right), \tag{19}$$

The perturbing Hamiltonian is often a periodic function in both ϑ and t variables, such that it can be Fourier-expanded to give

$$\mathcal{H}(\mathcal{I}, \vartheta, t) = \mathcal{H}_0(\mathcal{I}) + \epsilon\sum_{m=0}^{2m_0}\mathcal{H}_m^*(\mathcal{I})\cos(m\vartheta - n_0 t)\sum_{k=-\infty}^{+\infty}\delta\left(t - k\frac{2\pi}{N_a}\right), \tag{20}$$

where $\mathcal{H}_m^*$ are Fourier coefficients, whose detailed forms can be found in Ref. [21], and the perturbation strength is expressed by the parameter

$$\epsilon = -2\left(\frac{\ell}{2\pi R_0'}\right)\left(\frac{I_h}{I}\right), \tag{21}$$

which is usually small, since in experiments we have $\ell \ll 2\pi R'_0$ and $I_h \ll I_e$, where I_e is the coil current producing the toroidal equilibrium field.

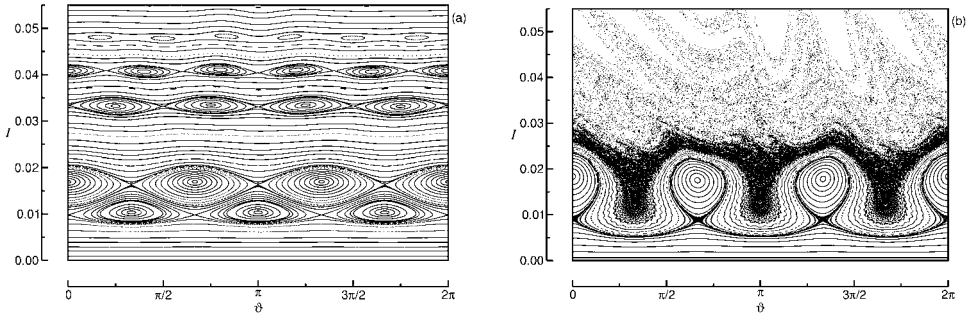

Figure 3. Poincaré maps (in action-angle variables) obtained through numerical integration of magnetic field line equations. The limiter current is (a) 0.70% and (b) 5.83% of the plasma current.

We integrated numerically the magnetic field line equations (18) and constructed Poincaré maps by sampling the field lines originating from many initial conditions when they cross the surface of section at $\varphi = 0$. For the sake of clarity we represented the Poincaré sections in rectangular plots of the action $\mathcal{I}$ and angle ϑ variables. Representative examples of exact Poincaré maps are shown in Figure 3 for different values of the limiter current.

For small perturbation amplitudes (low limiter currents), we observe two twin island chains near the shearless radius, with the resonant mode numbers $(3, 1)$ of the perturbation [Figure 3(a)]. Other islands are also visible corresponding to rational flux surfaces disturbed by the external magnetic field. Stronger perturbations can destroy some of these island chains, but not all of them, since the Hamiltonian system does not obeys KAM theorem (due to the non-monotonicity). For example, it is possible for the twin chains to approach each other without being destructed, as in usual stochasticity scenarios. The twin islands near the shearless radius first coalesce through a reconnection process and, secondly, undergo a saddle-center bifurcation which makes one of the twins to vanish, leaving in its place a highly complex chaotic region [Figure 3(b)]. This process has been thoroughly discussed in previous papers [16, 20, 21, 27].

3. Map for two resonant modes

Although the exact numerical integration of the magnetic field line equation yields Poincaré maps which reflects in a rather precise way the dynamics of the reconnecting and bifurcating islands in a negative shear equilibrium, it is a very time-consuming computational task. Many studies of long-term behavior of this system, as analyzes of diffusion, escape or loss of field lines would require a computationally fast and reliable scheme of numerical integration.

Instead of obtaining numerically the Poincaré maps, we can resort to the impulsive nature of the perturbation in (19) to obtain a local analytical approximation of the exact mapping [29]. The basic idea is to make an expansion of the canonical equations in the vicinity of the twin islands generated by the perturbation near the shearless radius r_s corresponding to mode number m_0.

Let us call $\mathcal{I}_1^*$ and $\mathcal{I}_2^*$ the action values corresponding to the two resonant radii r_1 and r_2, respectively, near the shearless radius. The equilibrium frequency at each rational surface is

$$\omega_0(\mathcal{I}_1^*) = \omega_0(\mathcal{I}_2^*) = \frac{\partial \mathcal{H}}{\partial \mathcal{I}} = \frac{n_0}{m_0} \tag{22}$$

where (m_0, n_0) are the mode numbers of the perturbation. Picking up from the model Hamiltonian (20) the resonant term corresponding to the frequency n_0/m_0 we get

$$\mathcal{H}(\mathcal{I}, \vartheta, t) = \mathcal{H}_0(\mathcal{I}) + \epsilon \mathcal{H}^*_{m_0}(\mathcal{I}) \cos(m_0\vartheta - n_0 t) \sum_{k=-\infty}^{+\infty} \delta\left(t - k\frac{2\pi}{N_a}\right), \tag{23}$$

We obtained a local approximation near the resonant modes m_0 by expanding (19) in the vicinity of the corresponding resonant radius $\mathcal{I}^*$ in powers of $\Delta\mathcal{I} = \mathcal{I} - \mathcal{I}^*$. After dropping the constant terms there results

$$\mathcal{H}(\mathcal{I},\vartheta,t) = \omega_0(\mathcal{I}^*)\Delta\mathcal{I} + \frac{1}{2}\left.\frac{d\omega_0}{d\mathcal{I}}\right|_{\mathcal{I}=\mathcal{I}^*}(\Delta\mathcal{I})^2 + \frac{1}{6}\left.\frac{d^2\omega_0}{d\mathcal{I}^2}\right|_{\mathcal{I}=\mathcal{I}^*}(\Delta\mathcal{I})^3 + \cdots \\ +\epsilon\mathcal{H}^*_{m_0}(\mathcal{I}^*_{1,2})\cos(m_0\vartheta - n_0 t)\sum_{k=-\infty}^{+\infty}\delta\left(t - k\frac{2\pi}{N_a}\right), \tag{24}$$

which can be further simplified by performing a canonical transformation to new action-angle variables $(\mathcal{I}',\vartheta')$ to eliminate the explicit time-dependence, through the generating function $S(\mathcal{I}',\vartheta,t) = \left(\vartheta - \frac{n_0}{m_0}t\right)\mathcal{I}'$, resulting in

$$\mathcal{H}'(\mathcal{I}',\vartheta') = \frac{\mathcal{M}}{2}\mathcal{I}'^2 - \frac{\mathcal{W}}{3}\mathcal{I}'^3 + K\cos(m_0\vartheta')\sum_{k=-\infty}^{+\infty}\delta\left(t - k\frac{2\pi}{N_a}\right), \tag{25}$$

where

$$\mathcal{M}(\mathcal{I}^*) \equiv \left.\frac{d\omega_0}{d\mathcal{I}}\right|_{\mathcal{I}=\mathcal{I}^*}, \quad \mathcal{W}(\mathcal{I}^*) \equiv \frac{1}{2}\left.\frac{d^2\omega_0}{d\mathcal{I}^2}\right|_{\mathcal{I}=\mathcal{I}^*}, \quad K(\mathcal{I}^*) \equiv \epsilon\mathcal{H}^*_{m_0}(\mathcal{I}^*_{1,2}) \tag{26}$$

Rescaling (25) by dividing by $\mathcal{M}$,

$$\mathcal{H}(\mathcal{I}',\vartheta') = \frac{1}{2}\mathcal{I}'^2 - \frac{\alpha}{3}\mathcal{I}'^3 + \kappa\cos(m_0\vartheta')\sum_{k=-\infty}^{+\infty}\delta\left(t - k\frac{2\pi}{N_a}\right), \tag{27}$$

where $\alpha = \mathcal{W}/\mathcal{M}$ and $\kappa = K/\mathcal{M}$. For notational convenience we denote $\kappa = \kappa_0 I_h$, where I_h is the limiter current.

However, taking only one resonant term from (19) is not enough to form a large chaotic region inside the tokamak plasma. Hence we also take into account a second resonant mode, namely (m_0+1, n_0), from the infinite number of possible Fourier harmonics in (19). Consideration of additional resonances would improve our description of the chaotic region, but they are not necessary to study the transport barrier in the shearless region, as aimed in the present work.

The derivation is similar for this additional mode, resulting on the addition of a perturbing term $\cos[(m_0+1)\vartheta']$ with strength $\tilde{\kappa} = \kappa_1 I_h$, κ_1 being the amplitude of the second resonant mode. The Hamilton equations for the local approximations read

$$\frac{d\mathcal{I}}{dt} = \left\{m_0\kappa\sin(m_0\vartheta') + (m_0+1)\tilde{\kappa}\sin[(m_0+1)\vartheta']\right\}\sum_{k=-\infty}^{+\infty}\delta\left(t - k\frac{2\pi}{N_a}\right), \tag{28}$$

$$\frac{d\vartheta'}{dt} = \mathcal{I}'(1-\alpha\mathcal{I}'). \tag{29}$$

The presence of a summation of periodic delta function enables one to integrate equations (28) and (29) by considering $\mathcal{I}'_k$ and ϑ'_k as the action and angle variables, respectively, just after the k-th kick, which occurs at time $t_k = N_r m_0$. This result in a discrete map

$$\mathcal{I}'_{k+1} = \mathcal{I}'_k + m_0\kappa\sin(m_0\vartheta'_{k+1}) + (m_0+1)\tilde{\kappa}\sin\left[(m_0+1)\vartheta'_{k+1}\right], \tag{30}$$

$$\vartheta'_{k+1} = \vartheta'_k + \frac{2\pi}{N_r}\mathcal{I}'_k(1-\alpha\mathcal{I}'_k) \qquad (mod 2\pi) \tag{31}$$

$$t_{k+1} = t_k + \frac{2\pi}{N_r}, \tag{32}$$

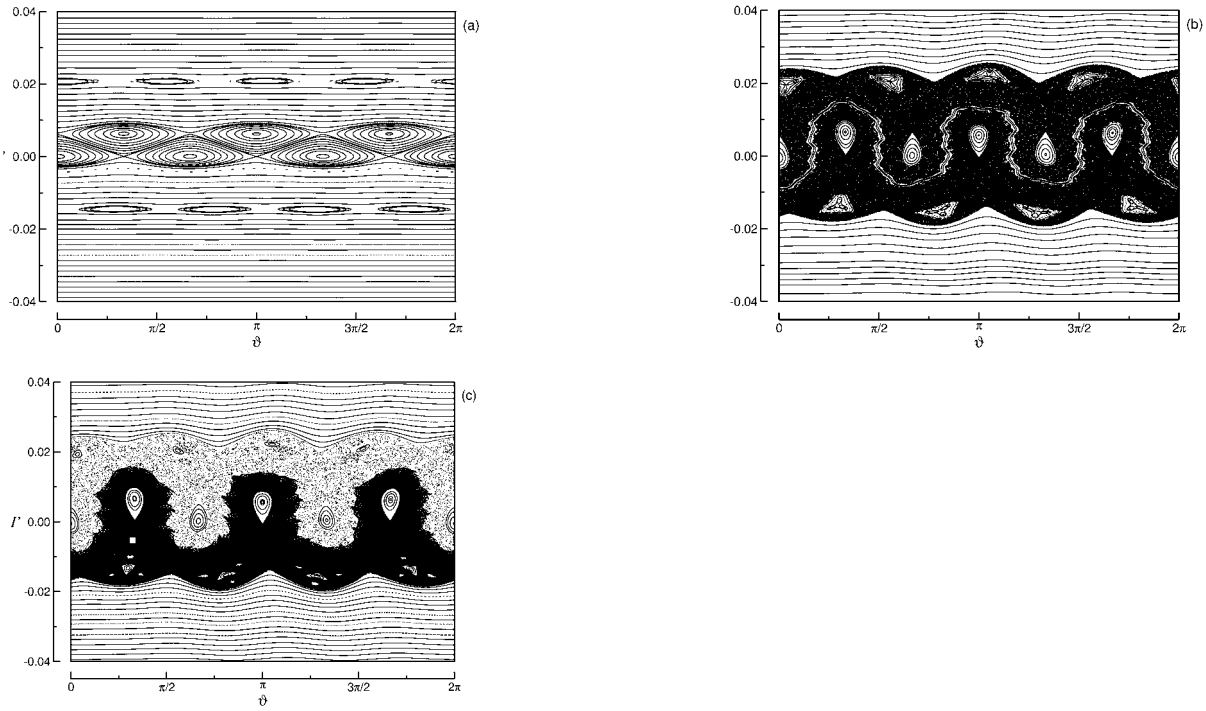

Figure 4. Phase portraits for the two-resonance mapping with (a) $\kappa_0 = 8.44 \times 10^{-6}$, $\kappa_1 = 3.88 \times 10^{-6}$; (b) $\kappa_0 = 1.48 \times 10^{-4}$, $\kappa_1 = 6.80 \times 10^{-5}$; (c) $\kappa_0 = 1.69 \times 10^{-4}$, $\kappa_1 = 7.77 \times 10^{-5}$.

4. Transport barrier

The numerical integration of the map obtained in the previous section is faster than of the exact Hamilton equations. Figure 4 shows typical phase portraits (using, as before, rectangular plots for the surfaces of section) obtained by means of the local map near two resonances.

The phase portrait depicted in Figure 4(a) shows a typical situation for small perturbation strengths of the two resonances, respectively given by $\kappa = \kappa_0 I_h$ and $\tilde{\kappa} = \kappa_1 I_h$. The first resonant mode $m_0 = 3$ generates two twin island chains near the shearless radius. For the chosen value of κ the islands are on the verge of mutually coalesce, the corresponding separatrices being practically reconnected. At the same time we observe the second twin island chain, corresponding to the resonant mode $m_0 + 1 = 4$. Due to the details of the safety factor profile, we still have two resonant radii, roughly symmetrically placed around the shearless radius. For a given limiter current, however, we have that $\tilde{\kappa} \ll \kappa$, so that the second mode has a width smaller than the first mode. The region in-between these two resonant modes is filled up with invariant tori of irrational flux surfaces which survive to the perturbation (note, however, that KAM theorem does not apply here, hence caution is needed to mathematically interpret these features).

In Fig. 4(a) the chaotic regions resulting from the non-integrability of the system are restricted to the vicinity of islands' separatrices and are too tiny to be visible due the a insufficient graphical resolution of the picture. However, as both perturbation strengths increase, such chaotic regions are enlarged and progressively engulf the invariant tori between resonances. The different resonances at each side of the shearless radius develop a global chaotic layer [Fig. 4(b)]. On the other hand, the two twin island chains nearer to the shearless radius undergo a reconnection process and, even for high perturbation strengths, have some invariant surfaces, a barrier, between the chaotic regions at each side of the shearless radius.

With a slightly higher perturbation these surviving surfaces eventually disappear, and a large chaotic region results comprising the entire region spanned by the two resonant modes sets in [Fig. 4(c)]. A detailed observation would show that the distribution of orbits in this chaotic region is far from being

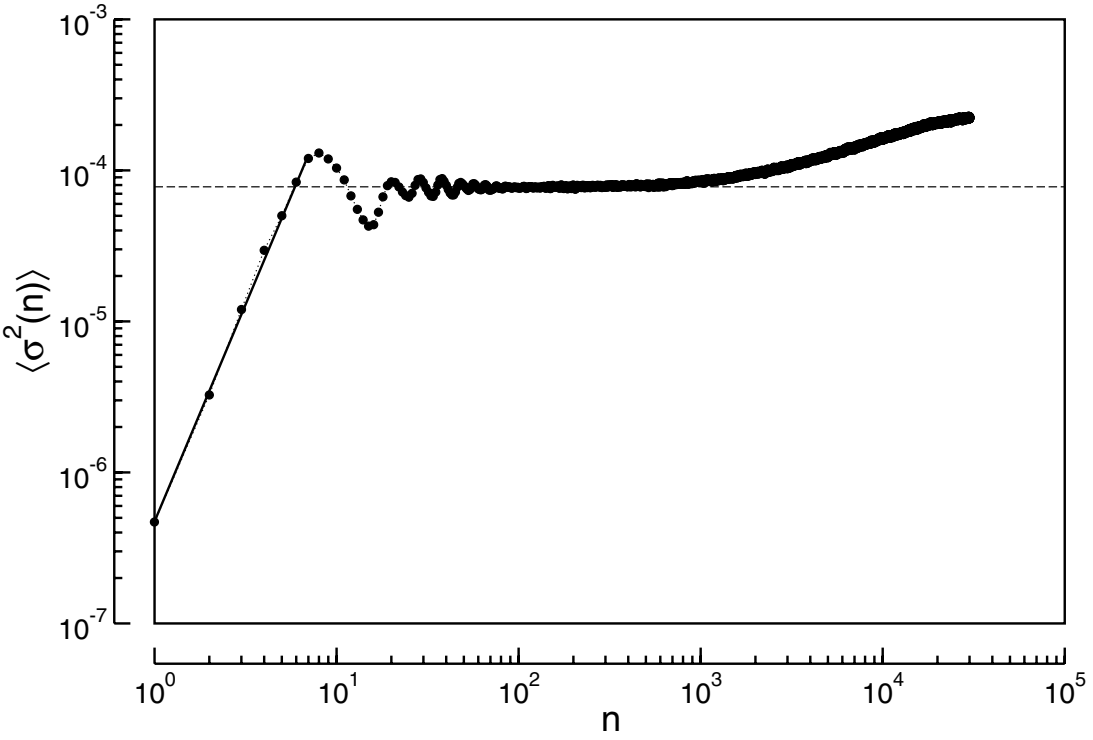

Figure 5. Average square displacement of the initial conditions within the small white depicted in Figure 4(c).

uniform, though. In Fig. 4(c) we picked up a small box (in white) from the core of the chaotic region and iterate the initial conditions therein a very large number of times. The density of points of the chaotic orbit can be roughly estimated from the concentration of pixels in the picture: the black (gray) regions are highly (poorly) visited. It turns out that the highly visited region is just the original chaotic region inside the shearless radius before the other chaotic regions have been reached.

We can interpret this result with one eye on the transport properties associated with chaotic motion. Since the trajectories become trapped for a long time before escaping to the other side of the shearless radius, we can regard the highly visited region as an effective transport barrier, since it hampers diffusion along this region. In order to give a quantitative verification of this statement, we take, in a phase portrait such as from Figure 4(c), a large number N_ϑ of initial conditions uniformly spread within a small box picked up from the core of the chaotic region. For each initial condition we compute the square displacement of the action variable and take an average over all the initial conditions:

$$< \sigma^2(n) > \equiv < (\delta \mathcal{I}_n)^2 >_i = \frac{1}{N_\vartheta} \sum_{i=1}^{N_\vartheta} (\mathcal{I}_{ni} - \mathcal{I}_{0i})^2, \tag{33}$$

If the actions were not restricted to a limited domain of the phase portrait, the average square displacement would depend with time as n^μ, where μ is positive exponent. Anomalous diffusion is characterized by $\mu \neq 1$, which we call sub or super-diffusive as $\mu < 1$ or $\mu > 1$, respectively. A uniform chaotic region is related to Gaussian diffusion, for which $\mu = 1$ [30, 31]. A time series of the average square displacement of the action is plotted in Figure 5, for $N_\vartheta = 10^4$ initial conditions chosen within the small white box in Figure 4(c).

Due to the existence of many invariant tori surrounding the chaotic region at both sides of the shearless curve, the maximal variation of the action variable is roughly 0.04. As far as we are analyzing the

behavior of the trajectories inside this region, we observe that the transport is initially super-diffusive, with σ_n^2 growing with time roughly as $n^{2.9}$. After less than a dozen iterations, however, the transport becomes sub-diffusive. In fact, the exponent is so small that for the ensuing $\sim 10^3$ iterations the average displacement does not change appreciably with time, indicating the presence of an effective transport barrier, as it could be guessed from Fig. 4(c). Iterating further the map equations, the average displacement resumes growing sub-diffusively with time, indicating that chaotic trajectories have escaped out of the broken transport barrier.

5. Conclusions

The formation of transport barriers in tokamaks with negative shear equilibria can be qualitatively explained by the non-twist nature of the resulting field line maps, when a chaotic region is formed inside the plasma column. The interpretation we give in this work to the mechanism underlying the appearance of an effective transport barrier is a trapping effect caused by the dynamical behavior of twin island chains appearing close to the shearless point. Such twin chains initially coalesce through a reconnective process and, as they interact with other neighbor islands, there appears a region of mostly chaotic behavior.

As a theoretical approach to reproduce this effect in numerical simulations, we derived in this paper an area-preserving analytical map for the field line flow. This map is non-twist thanks to the assumption of a non-monotonic profile for the safety factor of the equilibrium part of the model field. In order to generate the required chaotic layer inside the plasma column we have used an externally applied magnetic field due to an ergodic magnetic limiter. Our two-resonance map is thus capable to exhibit an effective transport barrier close to the shearless radius, even for high amplitude perturbations that destroy the barrier. With this map we can estimate the time required for a chaotic orbit to escape from this effective barrier. This barrier is relevant provided the duration of a typical tokamak plasma discharge is less than the average escape time.

Acknowledgments

This work was made possible with partial financial support of the following agencies: CNPq and FAPESP.

References

[1] J. P. Freidberg. *Ideal Magnetohydrodynamics* (Plenum Press, New York, 1987).
[2] J. Wesson. *Tokamaks* (Oxford University Press, 1987).
[3] H. Goedbloed, *Principles of Magnetohydrodynamics* (Cambridge University Press, 2004).
[4] P. J. Morrison, Rev. Mod. Phys. **70**, 467 (1998); Phys. Plas. **7**, 2279 (2000).
[5] H. Ali, A. Punjabi, A. Boozer, T. Evans, Plasma Phys. **11**, 1908 (2004).
[6] S. S. Abdullaev, Nucl. Fus. **44**, S12 (2004).
[7] A. J. Wooton, B. A. Carreras, H. Matsumoto, K. McGuire, W. A. Peebles, Ch. P. Ritz, P. W. Terry, and S. J. Sweben, Phys. Fluids B **2**, 2879 (1990).
[8] F. Wagner and U. Stroh, Plas. Phys. Contr. Fus. **35**, 1321 (1993).
[9] J. D. Meiss, Rev. Mod. Phys. **64**, 795 (1992).
[10] D. F. Düchs, A. Montvai, and C. Sack, Plas. Phys. Contr. Fus. **33**, 919 (1991).
[11] W. Horton, Rev. Mod. Phys. **71**, 735 (1999).
[12] F. M. Levinton, M. C. Zarnstoff, S. H. Batha, *et al.*, Phys. Rev. Lett. **75**, 4417 (1995).
[13] E. J. Strait, L. L. Lao, M. E. Manel, *et al.*, Phys. Rev. Lett. **75**, 4421 (1995).
[14] E. Mazzucato, S. H. Batha, M. Beer, *et al.*, Phys. Rev. Lett. **77**, 3145 (1996).
[15] R. Balescu, Phys. Rev. E **58**, 3781 (1998).
[16] D. Castillo-Negrete, J. M. Greene, and P. J. Morrison, Physica D **91**, 1 (1996).
[17] E. Petrisor, J. H. Misguich, and D. Constantinescu, Chaos, Solit. & Fract. **18**, 1085 (2003).
[18] J. E. Howard and S. M. Hohs, Phys. Rev. A **29**, 418 (1984).
[19] G. Corso, F. B. Rizzato, Phys. Rev. E **58**, 8013 (1998).
[20] E. Petrisor, Int. J. Bifurcat. Chaos **11**, 497 (2001).
[21] M. Roberto, E. C. da Silva, I. L. Caldas, R. L. Viana, Phys. Plasmas **11**, 214 (2004).
[22] F. Karger and F. Lackner, Phys. Lett. A **61**, 385 (1977).
[23] S. C. McCool, A. J. Wootton, A. Y. Aydemir, *et al.*, Nucl. Fus. **29**, 547 (1989).

[24] E. C. da Silva, I. L. Caldas, and R. L. Viana, IEEE Trans. Plas. Sci. **29**, 617 (2001); Phys. Plasmas **8**, 2855 (2001); Chaos, Solit. & Fract. **14**, 403 (2002).
[25] J. C. Vallet, L. Poutsschy, M. S. Mohammed-Benkadda, Phys. Rev. Lett. **67**, 2662 (1991).
[26] M. Y. Kucinski, I. L. Caldas, L. H. A. Monteiro, and V. Okano, J. Plas. Phys. **44**, 303 (1990).
[27] G. A. Oda and I. L. Caldas, Chaos, Solit. & Fract. **5**, 15 (1995); G. Corso, G. A. Oda, and I. L. Caldas, Chaos, Solit. & Fract. **8**, 1891 (1997).
[28] I. L. Caldas, R. L. Viana, M. S. T. Araujo, *et al.*, Braz. J. Phys. **32**, 980 (2002).
[29] M. Roberto, E. C. da Silva, I. L. Caldas, and R. L. Viana, Physica A **342**, 363 (2004).
[30] Y. Elskens and D. F. Escande, *Microscopic Dynamics of Plasmas and Chaos* (Institute of Physics Publishing, London, 2002).
[31] G. M. Zaslawsky, Phys. Rep. **371**, 461 (2002).